THE JOURNAL OF PHYSICAL CHEMISTRY C

Article

Cite This: J. Phys. Chem. C 2018, 122, 14447−14458

pubs.acs.org/JPCC

Highly Active Surface Structure in Nanosized Spinel Cobalt-Based Oxides for Electrocatalytic Water Splitting

Jing Zhou,[†,⊥] Jiong Li,[†,⊥] Linjuan Zhang,[†] Sanzhao Song,[†,‡] Yu Wang,[†] Xiao Lin,[†] Songqi Gu,[†] Xiang Wu,[§] Tsu-Chien Weng,[∥] Jianqiang Wang,*[,†,‡] and Shuo Zhang*[,†]

[†]Shanghai Institute of Applied Physics, Chinese Academy of Sciences, Shanghai 201204, P. R. China

[‡]University of Chinese Academy of Sciences, Beijing 100049, P. R. China

[§]State Key Laboratory of Geological Processes and Mineral Resources, China University of Geosciences, Wuhan 430074, P. R. China

[∥]Center for High Pressure Science & Technology Advanced Research, Shanghai 201203, P. R. China

Supporting Information

ABSTRACT: Spinel cobalt-based oxides are a promising family of materials for water splitting to replace currently used noble-metal catalysts. Identifying the highly active facet and the corresponding coordinated structure of surface redox centers is pivotal for the rational design of low-cost and efficient nanosized catalysts. Using high-resolution transmission electron microscopy and advanced X-ray techniques, as well as ab initio modeling, we found that the activity of Co^{3+} ions exhibits the surface dependence owing to the variability of its electronic configurations. Our calculation shows that the Co^{3+} site in {100} facet of nanosized $Li_2Co_2O_4$ exhibits an impressive intrinsic activity with low overpotential, far lower than that of the {110} and {111} facets. The unique, well-defined CoO_5 square-pyramidal structure in this nonpolar surface stabilizes the unusual intermediate-spin states of the Co^{3+} ion. Specially, we unraveled that oxygen ion anticipates the redox process via the strong hybridization Co 3d−O 2p state, which produces a $3d_{z^2}^{1.1}$ filling orbit. Finally, a spin-correlated energy diagram as a function of Co−O distance was devised, showing that the covalency of Co−O significantly affects the spin state of Co^{3+} ions. We suggest that the nonpolar surface that contains CoO_5 units in the edge-sharing systems with the short Co−O bond distance is a potential candidate for alkaline water electrolysis.

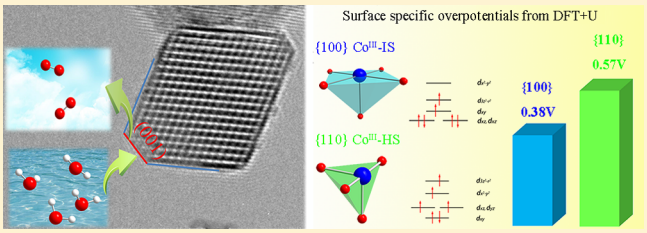

1. INTRODUCTION

The oxygen evolution reaction (OER) is a critical step in the energy conversion and storage, usually dominating the performance of fuel cells, water electrolyzers, photochemical solar cells, and metal−air batteries.[1−3] However, the kinetics of OER are sluggish, requiring the use of an electrocatalyst to overcome the high energy barrier of the O−O bond formation in commercial devices.[4,5] Currently, IrO_2 and RuO_2 have been identified as the most active catalysts for the OER, but the scarcity and high cost of each limit their wide application. Therefore, it is highly desirable yet challenging to develop an active and earth-abundant catalyst.[6] Among the wide variety of 3d transition metal oxides, spinel (AM_2O_4, M denoting transition metal) cobalt-based oxides, with "cubane"-like structure, are of particular interest, as they have intrinsic activities comparable to noble-metal catalysts, such as $NiCo_2O_4$,[7−9] $MnCo_2O_4$,[10,1110,11] Co_3O_4,[12−1412−14] and $Li_2Co_2O_4$.[15,16] These nanocatalysts exhibit morphology-dependent OER activities, implying that surface trivalent cobalt ions in different crystal planes possess a distinct intrinsic activity.[17−20] Therefore, identifying the active facet, which remains unknown for spinel cobalt-based oxides to date, is pivotal for the rational synthesis of efficient nanosized OER catalysts.

Generally, the different reactivity and selectivity of nanocatalysts depend greatly upon the different arrangements of surface atoms and the number of dangling bonds on different crystal planes.[21−23] The activity of cationic redox centers substantially dominates the performance of catalysts, and desirable catalysts bind reactants to the surface neither too strongly nor too weakly in terms of the Sabatier principle. The OER process involves four electron-transfer steps ($2H_2O \rightarrow O_2 + 4H^+ + 4e^-$), and accordingly, the binding strength for oxygen species is crucial. Unfortunately, the binding strength between oxygen molecules and reaction intermediate species is difficult to assess experimentally. Recently, experimental studies have revealed that transition-metal (TM) 3d-band electron occupation correlates with adsorption energy and, in turn, reactivity.[24] In particular, the occupancy of 3d electrons with e_g symmetry of trivalent ions is the most important, and

Received: January 12, 2018
Revised: May 17, 2018
Published: June 7, 2018

DOI: 10.1021/acs.jpcc.8b00407
J. Phys. Chem. C 2018, 122, 14447−14458

OER performance exhibits a volcano-shaped dependence on this property, i.e., e_g unit occupancy oxides present peak activity. Suntivich et al. explained that it is essentially with relation to the two contrary rate-determining steps that *OH and *OOH species adsorption and unit 3d-e_g filling ions could provide mediated adsorption ability for these reaction intermediates.[25,26] Fundamentally, such correlations between Co 3d occupancy and catalytic performance illustrate a spin-dependent OER reactivity. The e_g unit occupancy of Co^{3+} ions requires that the trivalent cobalt ion possess an intermediate spin (IS) state ($t_{2g}^5e_g^1$, $S = 1$).[17] Although this spin-correlated descriptor has become a widely accepted design principle for OER catalysts and is usually employed to explain the origin of good catalytic performance,[27−29] the IS state of Co^{3+} ions is uncommon and little robust experimental evidence regarding it has been reported to date.

According to the available data, the trivalent cobalt ions can be of low spin (LS, $t_{2g}^6e_g^0$, $S = 0$), high spin (HS, $t_{2g}^4e_g^2$, $S = 2$), and even intermediate spin (IS, $t_{2g}^5e_g^1$, $S = 1$),[30] mainly depending on the coordinated environment symmetry and Co−O bond length. Most of the crystal structures of trivalent cobalt oxides contain a CoO_6 octahedron, in which the Co^{3+} ion primarily presents an LS state, such as $NaCoO_2$,[31] $LiCoO_2$,[32] and $EuCoO_3$,[33] and an HS state has rarely been found, but $SrCo_{0.5}Ru_{0.5}O_{3-\delta}$ was reported in recent work.[34] An HS state of the Co^{3+} ion was also found in a mixed-valence cobalt oxide $YBaCo_4O_7$[35] with CoO_4 tetrahedral symmetry and in Sr_2CoO_3Cl[36] and $BiCoO_3$[37] with a pyramidal CoO_5 coordinated environment. In contrast to the bulk that possesses rigid crystal structure, a surface has a flexible structure that usually provides reduced coordinated environments, such as 5-fold pyramidal[38,39] or 4-fold pseudo-tetrahedral,[40] leading to a distinct electronic configuration of the active sites. Thus, capturing the characteristic CoO_x surface structure for high OER activity is crucial for the design of highly active, nanosized cobalt-based catalysts. A systematic investigation of the fundamental, atomic-scale catalytic properties of these reactions on well-characterized materials is therefore mandatory.

In the present study, we selected nanosized $Li_2Co_2O_4$ as a model for spinel cobalt oxides to identify the highly active facet and suitable electronic configuration of catalytic sites for OER; in particular, to establish the intrinsic correlation between characteristic surface structures and the spin state of Co^{3+} ions. $Li_2Co_2O_4$ material is a desirable system for this study to exclude the complexities inherent in Co_3O_4, which contains mixed-valence states of cobalt ions, and in $MnCo_2O_4$ or $NiCo_2O_4$, both of which generally possess inverse spinel structure in which partial cobalt ions occupy the tetrahedral sites. Herein, we used high-resolution transmission electron microscopy (HRTEM) combined with density functional theory (DFT) calculations to identify the shape and expose the crystal planes, as well as the percentage of each facet. We then determined the spin state of Co^{3+} ions in each facet by calculating the spin-correlated surface free energy. This theoretical result is further evidenced by depth-profiling advanced synchrotron-radiation X-ray spectroscopy. Next, thermodynamics calculations were employed to assess the contribution of each facet to OER activity. We identified that the {100} surface plane has a dominant contribution for superior OER catalytic performance of this system. Specially, we observed that oxygen ions directly anticipate the redox process via Co 3d−O 2p hybridization.

2. EXPERIMENTAL AND CALCULATIONAL SECTION

2.1. Synthesis and Characterization. Powder samples of nanosized $Li_2Co_2O_4$ were prepared by a sol−gel reaction method following a previously published procedure.[16] IrO_2 was purchased from Alfa Aesar and Co_3O_4 was prepared by a hydrothermal method in a previous study.[41] The crystalline structure of the sample was analyzed by X-ray diffraction on a D8-Advance Bruker-AXS diffractometer using Cu Kα irradiation and Raman spectra recorded in the backward geometry on a NIHON BUNKO Ventuno spectrometer (NSR-1000DT). The sample morphology was characterized by high-resolution transmission electron microscopy (HRTEM) on a Tecnai G2 F20 S-TWIN microscope and by high-angle annular-dark-field (HAADF) scanning transmission electron microscopy (STEM) using an aberration-corrected Titan G2 60-300 microscope operated at 300 kV. The STEM convergence semi-angle was approximately 21.4 mrad. The spatial resolution of STEM is ∼0.07 nm, which offers an unprecedented opportunity to probe structures with a sub-angstrom resolution. The valence state of cobalt ions was obtained by X-ray photoelectron spectroscopy (XPS) on a Kratos Axis Ultra DLD using a 1486.6 eV Al Kα source. Magnetization measurements were performed with a superconducting quantum-interference device (SQUID, Quantum Design) in the temperature range 2−300 K.

2.2. Electrochemical Measurements of OER Activities. The electrochemical measurements of all the samples were carried out under the same test conditions. Typically, 5 mg of electrocatalyst powder and 5 mg of carbon black were dispersed in 1 mL of 1:1 (v/v) deionized water/isopropanol mix solvent with a 40 μL Nafion solution (5 wt %, Sigma-Aldrich). The mixture was sonicated in an ultrasonic water bath for approximately 1 h to form a homogeneous catalyst ink. Next, 10 μL of the ink was coated onto a glassy carbon disk with a diameter of 5 mm, at a loading rate of approximately 0.25 mg_{oxide}/cm^2, and dried at room temperature. The glassy carbon disk electrode was polished with different polishing powders (1.0 and 0.3 μm α alumina and 50 nm γ alumina, in order) and thoroughly cleaned with deionized water and ethanol before loading. All the electrochemical measurements were performed in O_2-saturated 1 M KOH with conventional three electrodes on an Auto Lab electrochemical station in which saturated HgO/Hg and platinum wires were used as the reference and counter electrodes, respectively. Linear sweeping voltammograms (LSVs) and cyclic voltammetry were obtained at a scan rate of 5 and 1 mV/s, respectively. Electrochemical impedance spectroscopy (EIS) was run with alternating current (ac) voltage with 10 mV amplitude at a potential of 1.58 V versus reversible hydrogen electrode (RHE) within the frequency range 0.1 Hz to 100 kHz. All the potentials were corrected to compensate for the effect of solution resistance measured via high-frequency ac impedance.

2.3. Synchrotron Radiation X-ray Spectroscopy Measurements. The Co K-edge extended X-ray absorption fine-structure (EXAFS) data were measured at the beamline 14 W of the Shanghai Synchrotron Radiation Facility (SSRF). The measurement was carried out with a Si(111) double-crystal monochromator in the transmission mode. The Co $L_{2,3}$-edge X-ray absorption spectroscopy (XAS) spectra were collected at room temperature at beamlines BL08B and BL09A2 of the National Synchrotron Radiation Research Center (NSRRC) in Taiwan, with a photon energy resolution

DOI: 10.1021/acs.jpcc.8b00407
J. Phys. Chem. C 2018, 122, 14447−14458

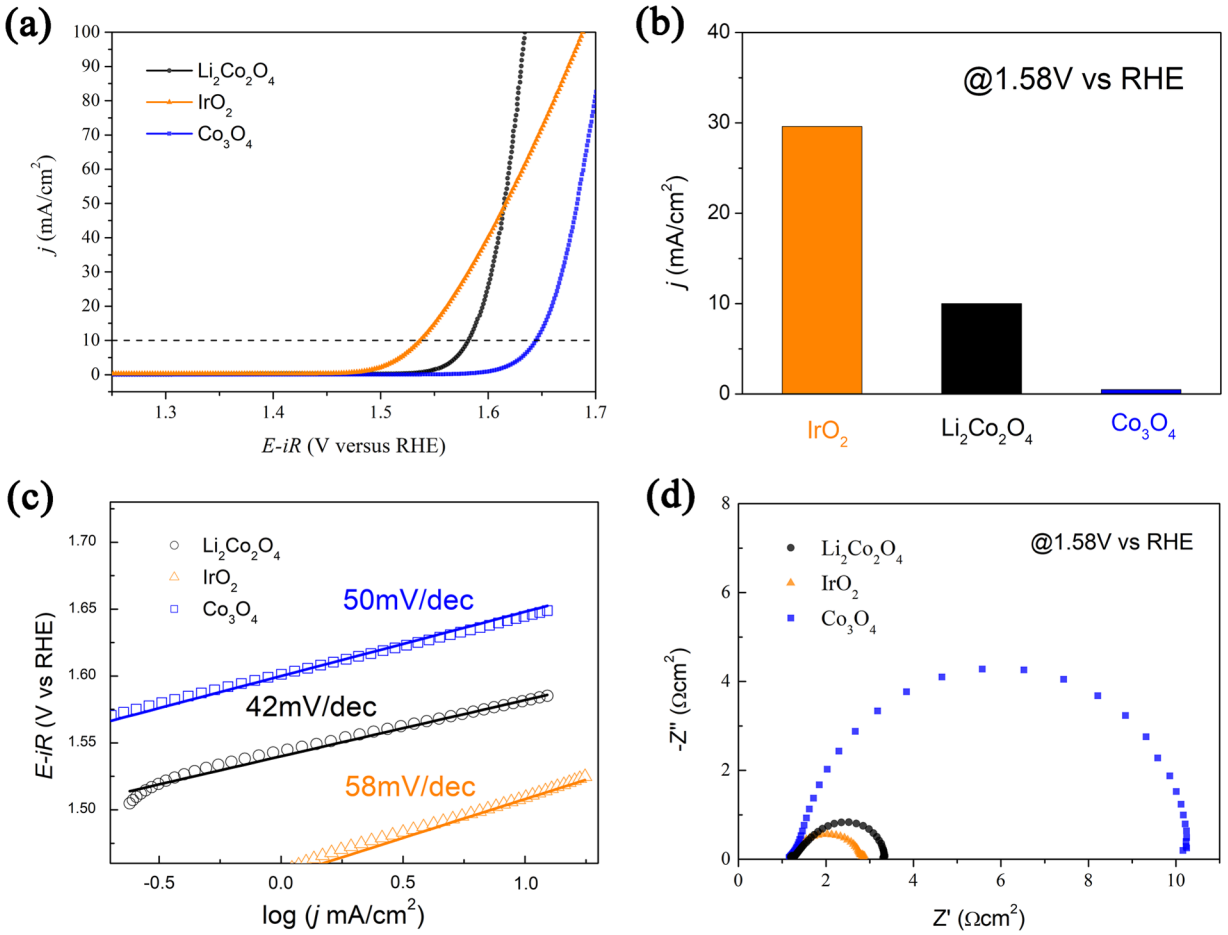

Figure 1. (a) Linear sweep voltammograms at a scan rate of 5 mV/s, (b) current density at 1.58 V (vs RHE), (c) Tafel plots, and (d) electrochemical impedance spectroscopy (EIS) recorded at 1.58 V (vs RHE) under the influence of an ac voltage of 10 mV of $Li_2Co_2O_4$, IrO_2, and Co_3O_4 at 1600 rpm in O_2-saturated 1 M KOH solution.

of approximately 0.15 and 0.3 eV, respectively. The pellet sample was fractured in situ in an ultrahigh-vacuum chamber with a pressure in the 10^{-10} mbar range. The spectra were recorded in the total electron yield (TEY) and Auger electron yield (AEY) modes. The sample drain current was collected for TEY. AEY was collected with a cylindrical mirror analyzer using a pass energy of 200 eV.

2.4. Density Functional Theory Calculations. The surface structure optimized and surface energy calculations were carried out using the Vienna ab initio simulation package.[42,43] All the spin-polarized DFT calculations were performed using projector-augmented wave pseudopotentials and the revised-Perdew–Burke–Ernzenhof exchange correlation functional. The Hubbard U model was applied for a better description of the Co 3d electrons, and the value of U_{eff} was set to be 3.52 eV according to the previous work.[44] Periodic slab calculations were carried out using a plane-wave energy cutoff of 500 eV and a vacuum spacing of approximately 20 Å. The experimental lattice constants were adopted. All the surface structural models had a minimum of 12 atomic layers and a 1 × 1 cell sampled by a 5 × 5 × 1 Monkhorst–Pack k-points mesh. The geometries were relaxed until a maximum threshold force of 0.01 eV/Å was fulfilled.

The theoretical overpotentials for $Li_2Co_2O_4$ surfaces were calculated based on the conventional single-site OER mechanism.[44] Four elementary steps are considered on the basis of an acidic environment

$$2H_2O + * \rightarrow OH^* + H_2O + e^- + H^+ \quad (1)$$

$$H_2O + OH^* \rightarrow O^* + H_2O + e^- + H^+ \quad (2)$$

$$H_2O + O^* \rightarrow OOH^* + e^- + H^+ \quad (3)$$

$$OOH^* \rightarrow O_2 + e^- + H^+ \quad (4)$$

Thus, the Gibbs free energy differences can be expressed as

$$\Delta G_1 = \Delta G_{OH} - eU + \Delta G_{H^+}(pH) \quad (5)$$

$$\Delta G_2 = \Delta G_O - \Delta G_{OH} - eU + \Delta G_{H^+}(pH) \quad (6)$$

$$\Delta G_3 = \Delta G_{OOH} - \Delta G_O - eU + \Delta G_{H^+}(pH) \quad (7)$$

$$\Delta G_4 = 4.92 - \Delta G_{OH} - eU + \Delta G_{H^+}(pH) \quad (8)$$

where 4.92 eV is the experimental Gibbs free energy of formation of two water molecules and $\Delta G_{H^+}(pH)$ is represented by the Nernst equation as $\Delta G_{H^+}(pH) = -k_B T \ln(10) \times pH$. The Gibbs free energy differences are calculated using the computational standard hydrogen electrode model. ΔG_{OH}, ΔG_O, and ΔG_{OOH} are calculated in standard conditions when pH = 0 and U = 0, so the last two terms from each expression above are equal to zero. Zero point energy and entropy corrections are also considered according to the previous work.[44]

DOI: 10.1021/acs.jpcc.8b00407
J. Phys. Chem. C 2018, 122, 14447–14458

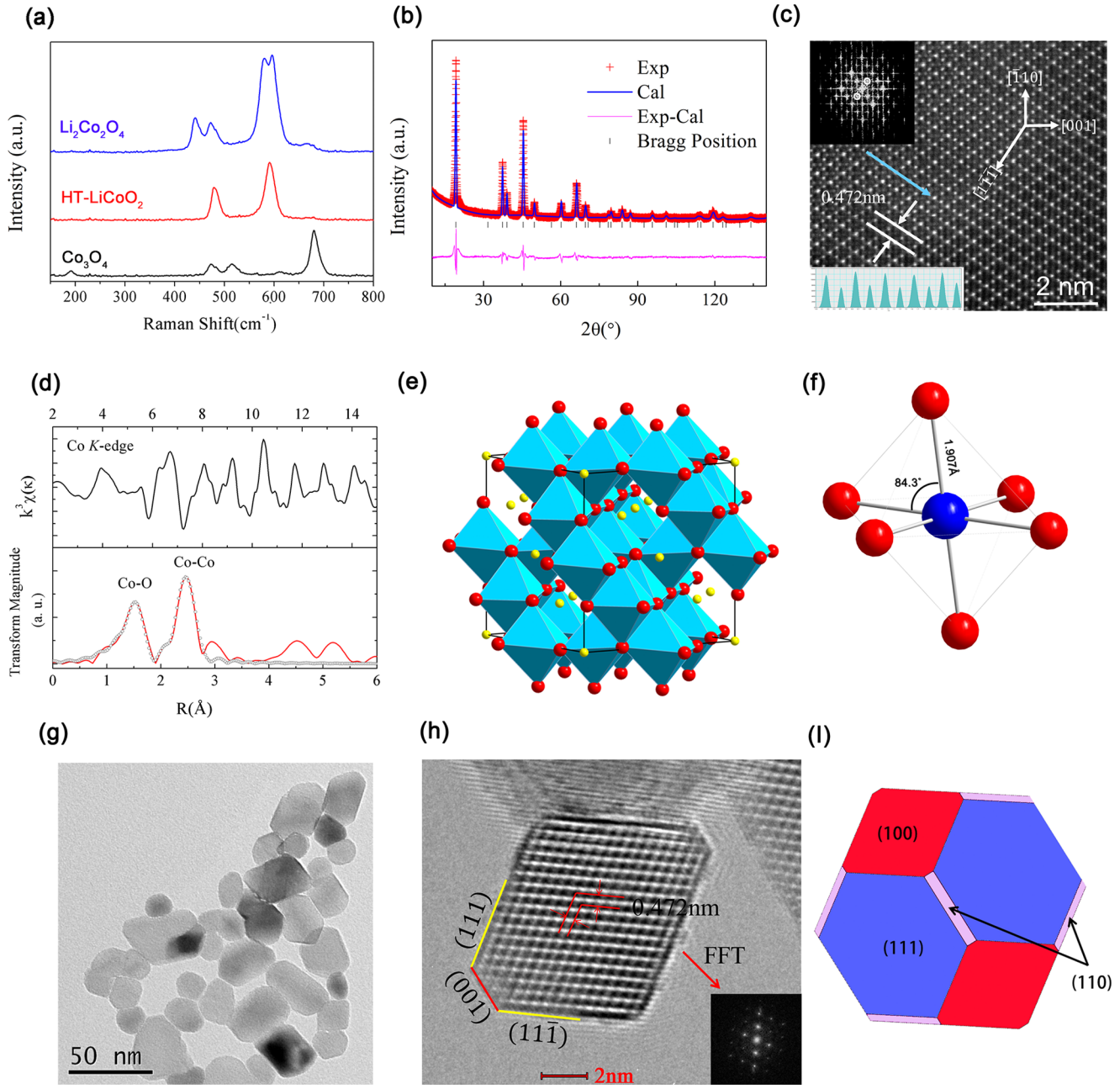

Figure 2. (a) Raman spectra for $Li_2Co_2O_4$ along with $LiCoO_2$ and Co_3O_4 for comparison. (b) XRPD pattern with experimental data denoted by red crosses, calculated curve in blue, and difference curve in purple. (c) HAADF-STEM images of $Li_2Co_2O_4$ viewed down the [110] zone axis. (d) *k*-Weighted EXAFS $\chi(k)$ function and Fourier transform at the Co K edge for $Li_2Co_2O_4$. (e) Framework crystal structure. (f) CoO_6 octahedron of $Li_2Co_2O_4$. Li, Co, and O atoms are shown by purple, blue, and red spheres, respectively. (g) TEM images of $Li_2Co_2O_4$ nanoparticles. (h) HRTEM images viewed along the [1 $\bar{1}$ 0] orientations with inserted microdiffraction patterns. (i) Predicted equilibrium crystal morphology for $Li_2Co_2O_4$ nanoparticle using Wulff construction.

Finally, the theoretical overpotential η_{theory} can be defined from the Gibbs free energy differences at each step

$$\eta_{theory} = \frac{\max[\Delta G_1, \Delta G_2, \Delta G_3, \Delta G_4]}{e} - 1.23\ \text{V} \quad (9)$$

It is worth mentioning that this approach is also applicable to an alkaline environment because the intermediates are the same in both acidic and alkaline environments.

2.5. Transition-Metal $L_{2,3}$-Edge XAS Spectra Simulation. The simulation of transition-metal (TM) $L_{2,3}$-edge XAS spectra were performed by employing the successful configuration interaction cluster model that includes the full atomic multiplet theory and hybridization with the O 2p ligands.[45] This approach includes both electronic Coulomb interactions and spin−orbit coupling for each subshell, in addition to Hartree−Fock estimates of the radial part of the matrix elements of the Coulomb interaction in terms of Slater integrals F^k and G^k and the spin−orbit coupling parameters $\zeta(2p)$ and $\zeta(3d)$ for the core 2p and valence 3d valence shells. The hybridization of the TM 3d orbit and O 2p orbit is treated using a charge-transfer model, in which the $3d^{n+1}\underline{L}$ ($\underline{L}$ denotes a ligand hole) and $3d^{n+2}\underline{L}^2$ configurations above the $3d^n$ configuration are involved. The energy difference of these configurations is defined using the charge-transfer energy Δ

DOI: 10.1021/acs.jpcc.8b00407
J. Phys. Chem. C 2018, 122, 14447−14458

and the 3d−3d Coulomb interaction U_{dd}. In this model, the ground states φ can be written as $\varphi = \alpha|3d^n> + \beta|3d^{n+1}\underline{L}> + \gamma|3d^{n+2}\underline{L}^2>$.

3. RESULTS AND DISCUSSION

3.1. Electrochemical Performance. The electrochemical performance of the studied systems is shown in Figure 1 and Table S1. The OER catalytic activities of prepared $Li_2Co_2O_4$ and reference samples were evaluated by linear sweeping voltammogram (LSV) measurements in a 1.0 M KOH aqueous solution using a typical three-electrode cell setup, as shown in Figure 1a. All the potential values are *iR*-corrected during each LSV to compensate for the resistance of the solution. It is important to compare the relative values of the overpotential η required to achieve a current density of 10 mA/cm^2, which is a metric relevant to solar fuel synthesis. Remarkably, the $Li_2Co_2O_4$ catalyst affords such a current density at a comparably small η value (approximately 0.35 V), which is more negative than that of nanoparticle Co_3O_4 showing the same morphology, as illustrated in Figure 1a,b. Such an activity of $Li_2Co_2O_4$ is excellent among those of most state-of-the-art, highly active cobalt-based OER electrocatalysts that have been reported in the literature, as shown in Table S2. In addition, the current density of $Li_2Co_2O_4$ sharply increases with increasing potential; for instance, it is nearly 90 mA/cm^2 at 1.63 V, extensively larger than that of IrO_2, as shown in Figure S1. The Tafel plots of three catalysts as drawn in Figure 1c show that the Tafel slopes are 42, 50, and 54 mV/dec (millivolts per decade of electrical current density) for $Li_2Co_2O_4$, Co_3O_4, and IrO_2, respectively. The $Li_2Co_2O_4$ catalyst exhibits the smallest Tafel slope among the studied materials. The charge-transfer resistances were determined by electrochemical impedance spectroscopy (EIS) measurements, as displayed in Figure 1d. The smaller charge-transfer resistance (R_{ct}) value of $Li_2Co_2O_4$ means that it possesses a faster charge-transfer rate than Co_3O_4 during the OER process.

3.2. Crystal Structure and Morphology. The crystal structures of the prepared $Li_2Co_2O_4$ sample were characterized by Raman, X-ray powder diffraction (XRPD), and extended X-ray absorption fine structure (EXAFS). The Raman pattern as shown in Figure 2a exhibits four peaks corresponding to the $A_{1g} + E_g + 2F_{2g}$ active modes, indicating a standard *Fd*3*m* symmetry of our sample.[46] No impurity phase, such as layered $LiCoO_2$ or Co_3O_4, can be detected. The measurement and calculated XRPD patterns of $Li_2Co_2O_4$ are shown in Figure 2b. Rietveld refinement revealed that $Li_2Co_2O_4$ possesses a cubic structure with lattice parameters of a = 7.9825(4) Å and a space group of *Fd*3*m* (see Table S3). The cubic phase structure was further confirmed by aberration-corrected HAADF-STEM, as shown in Figure 2c, viewed along the [110] orientations. The $Li_2Co_2O_4$ system adopts a lithiated spinel structure $\{Li_2\}_{16c}[Co_2]_{16d}O_4$ in which the Co^{3+} ions occupy all the 16d CoO_6 octahedral sites, whereas the Li^+ ions occupy all the 16c LiO_4 tetrahedral sites of the framework. Slightly distorted CoO_6 octahedrons were found, and they form a framework by edge sharing in this system, as plotted in Figure 2e,f. The bond angle of Co−O−Co is nearly 90° and accordingly leads to a short Co−Co distance, in contrast to perovskite oxides, which possess 180° of the bond angle of Co−O−Co.

The Co−O bond length plays a central role in affecting the valence and spin state of cobalt ions. The XRPD refinement results identified the value of 1.907 Å, which is further confirmed by Co K-edge EXAFS data fitting (see Table S4). It is a very small value among the trivalent cobalt oxides with a CoO_6 coordination environment—not only extensively smaller than that in HS systems, such as 1.98 Å in $SrCo_{0.5}Ru_{0.5}O_{2.96}$[34] and 1.961 Å in $LaCoO_3$ at 1000 K,[47] but also even smaller than that in mostly LS systems, e.g., 1.925 Å in $LaCoO_3$ at 5 K,[47] 1.922 Å in $LiCoO_2$,[4848] and 1.918 Å in $Ca_3Co_2O_6$.[4949] With such a short distance, the bulk Co ions within the CoO_6 octahedrons are subjected to crystal-field strength that sufficiently large to stabilize the nonmagnetic LS state. However, the Co ions at the surface possess reduced coordinated environments, such as 5-fold pyramids or 4-fold pseudo-tetrahedrons, which, in turn, could have a different spin state due to the redistribution of 3d electrons.

The morphology of the spinel $Li_2Co_2O_4$ was studied by TEM and HRTEM. Figure 2g shows that the as-synthesized nanoparticles present a cubo-octahedral shape, and that the average size is approximately 20 nm. The HRTEM image is viewed along the [1 $\bar{1}$ 0] orientation. The lattice fringe distance was measured to be 4.72 Å, corresponding to the {111} facet. Hence, the dominant exposed planes are {111} and {100}. In attempts to further estimate the percentage of these exposed facets, the equilibrium particle shape was constructed using the Wulff method with the help of the calculated surface free energies as listed in Table 1, considering the three low index surfaces {111}, {100}, and {110}. It was found that {111} is the most energy-stable surface facet, which accounts for the 64.3% of the entire surface area. In turn, the {100} surface contributes 29.64%. The {110} surface has the largest surface energy and only accounts for 6.06%.

Table 1. Surface Energy of Facets Dependent on Co^{3+} Spin State

surface	coordination no. of oxygen	γ (J/m^2) with HS	γ (J/m^2) with IS	γ (J/m^2) with LS
{100}	5/6	1.601	1.087	1.547
{111}	6	2.714	1.356	1.005
{110}	4/6	2.202	2.493	2.947
	6	1.352	1.212	1.187

3.3. Surface Properties and Spin State of Co^{3+} Ions. Because the surface cobalt ions have been typically regarded as the adsorption site and redox center allowing the electron transfers during water oxidation, we further gained insight into their electronic configuration at different exposed facets. The DFT results indicate that all cobalt ions of three facets are trivalent valence state, as shown in Figure S9. In contrast, the spin state shows a facet dependence. There are different coordinate environments of the central metal in different facets of the crystal. It may cause the change in the surface crystal field and covalency strength of metal−oxygen bonding, which can further influence the arrangement of orbital energy levels and may result in the change in the electronic spin state on the different facet. Surface energies calculated with specific surface structures and spin states provide an important criterion to determine the most stable surface structure and spin state.[39] The crystal-field splitting of 3d orbitals and the corresponding energy levels of Co^{3+} ions with different coordinated environments are plotted in Figure 3. The {111} facet is a polar plane and has two possible surface terminations, i.e., an O-terminated or Li/Co-terminated structure, as shown in Figure S9. The former is energy favorable and the optimized

DOI: 10.1021/acs.jpcc.8b00407
J. Phys. Chem. C 2018, 122, 14447−14458

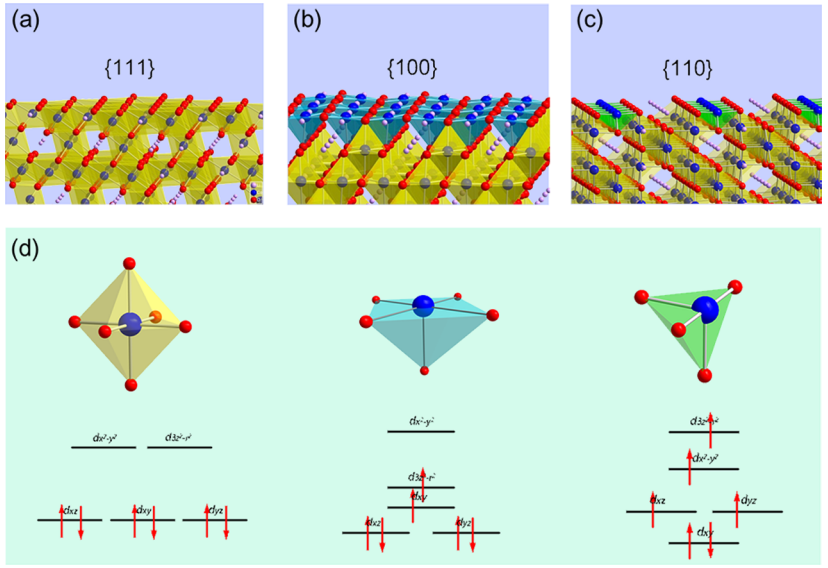

Figure 3. (a) {111}, (b) {100}, and (c) {110} surfaces of $Li_2Co_2O_4$. (d) Octahedrally, square pyramidally, and pseudo-tetrahedrally coordinated Co ions and the corresponding electronic configurations. (Red spheres, oxygen; purple, lithium; blue, cobalt.)

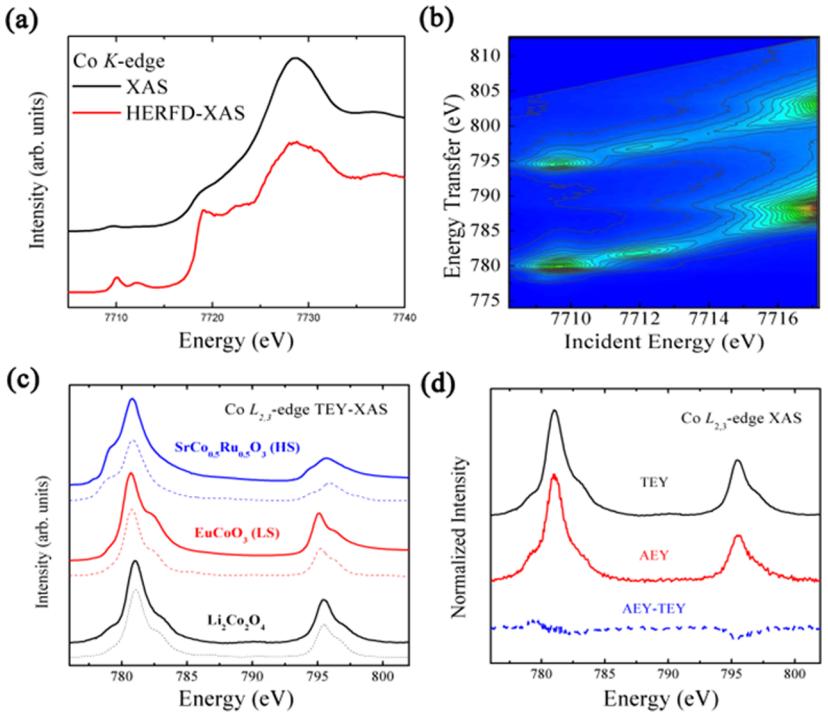

Figure 4. (a) High-energy-resolution fluorescence-detected (HERFD) spectrum of Co K edge and (b) 1s2p RXES plane for $Li_2Co_2O_4$. (c) Experimental (solid line) and calculated (dashed line) Co $L_{2,3}$ edge TEY-XAS spectra of $Li_2Co_2O_4$ along with $EuCoO_3$ and $SrCo_{0.5}Ru_{0.5}O_3$ for comparison. (d) Experimental Co $L_{2,3}$ edge TEY and AEY-XAS spectra of $Li_2Co_2O_4$, and the difference curve in blue below them.

surface structure as shown in Figure 3a clearly reveals that CoO_6 octahedrons are preserved and, importantly, no cobalt ions are exposed on the surface. Co^{3+} ions on this surface possess a LS ($t_{2g}^6e_g^0$, $S = 0$) state. The surface energy is 1.005 J/m^2, which is remarkably lower than that of IS (1.356 J/m^2) and HS (2.714 J/m^2) configurations. In contrast, the {100} is a nonpolar plane and has only one Li/Co/O-terminated pattern. The optimized surface structure is plotted in Figure 3b, from which we note that cobalt ions are exposed on the surface and in the CoO_4 basal planes, forming CoO_5 square pyramids. Notably, the Co^{3+} ions exhibit an IS ($t_{2g}^5e_g^1$, $S = 1$) state, in which the d_{z^2} orbit is unit occupied. The surface energy calculation indicates that the IS configuration (1.087 J/m^2) is highly stable compared to the LS configuration (1.547 J/m^2). Finally, the {110} surface has three possible terminated configurations, as plotted in Figure S9. The most stable structure of the {110} surface is nearly identical to the LS configuration of the {111} surface with a CoO_6 octahedron. For the other two possible configurations, however, the Co^{3+} ion is bare on the surface and in a 4-fold pseudo-tetrahedral structure, which stabilizes the HS ($t_{2g}^4e_g^2$, $S = 2$) state, as shown in Figure 3c.

DOI: 10.1021/acs.jpcc.8b00407
J. Phys. Chem. C 2018, 122, 14447−14458

Table 2. Calculated Adsorption Energies, Gibbs Free Energy Changes (in Electronvolts), and Overpotentials (in Volts) for the Surface of $Li_2Co_2O_4$

surface		ΔE_O	ΔE_{OH}	ΔE_{OOH}	ΔG_1	ΔG_2	ΔG_3	ΔG_4	η
{100}		2.77	0.83	3.67	1.27	1.60	1.34	0.71	0.38
{110}	T_1	1.95	0.34	3.31	0.78	1.27	1.80	1.07	0.57
	T_2	2.92	0.53	3.22	0.97	2.05	0.74	1.16	0.82

To further distinguish the spin state of Co^{3+} ions in bulk and at the surface region, we performed the measurements with different probing depth abilities. First, bulk-sensitive high-energy-resolution fluorescence-detected (HERFD)-XAS and 1s2p resonant X-ray emission spectroscopy (RXES) measurements were performed, as shown in Figure 4a,b. Their spectral behaviors are similar to those of the LS-Co^{3+} ions,[50] illustrating that trivalent cobalt ions in bulk possess a LS state. This conclusion is also supported by the "L-like" spectra derived by cutting the RXES plane (see Figure S13). The surface-sensitive Co $L_{2,3}$ edge XAS were measured with TEY and AEY modes, which have typical probing depths of ∼5 and ∼1 nm, respectively. The line shape of the TM $L_{2,3}$-edge spectra strongly depends on the multiplet structure given by the TM 3d−3d and 2p−3d Coulomb and exchange interactions, as well as by the local crystal fields and the hybridization with the O 2p ligands.[31,51−53] This makes the technique extremely sensitive to the spin, orbital, and valence states of the ions. Figure 4c depicts the TEY-XAS of $Li_2Co_2O_4$ and of reference single-crystal samples including $SrCo_{0.5}Ru_{0.5}O_{2.96}$ and $EuCoO_3$, which represent 6-fold octahedral HS-Co^{3+} and LS-Co^{3+}, respectively.[33,34] To date, no pure IS-Co^{3+} references have been reported. In the spectrum of $EuCoO_3$, we note that a shoulder feature appears in the higher-energy region above the main peak both for L_3 and L_2 peaks. This is a characteristic of LS-Co^{3+} that can be found in the Co $L_{2,3}$-edge XAS of $NaCoO_2$, $LiCoO_2$, and $LaCoO_3$ (measured at 5 K) systems. In contrast, the shoulder feature in the spectrum of $SrCo_{0.5}Ru_{0.5}O_{2.96}$ locates in the lower-energy region both for L_3 and L_2 peaks. This HS-Co^{3+} characteristic can also be seen in $LaCoO_3$ (measured at 650 K) and even in Sr_2CoO_3Cl,[36] a HS-Co^{3+} system with a CoO_5 pyramidal coordinated environment. A typical LS state character can be observed in the TEY-XAS, indicating that the Co ions in the near-surface region still remain in the LS state. In contrast, the AEY spectrum exhibits distinct features, as displayed in Figure 4d. Compared to that in TEY-XAS, the peak at 779 eV gains more intensity and the features in the L_2 regions lose intensity in AEY-XAS. Moreover, we performed theoretical simulations of Co $L_{2,3}$-edge spectra, and it was found that the superposition of 75% CoO_6 signal and 25% CoO_5 signal well reproduces the AEY-XAS spectrum (see Figure S14), proving that the partial Co^{3+} ions at the surface possess a higher spin state. This existence of dangling bonds is also evidenced by the magnetic susceptibility data (see Figure S15).

3.4. Thermodynamics of Water Oxidation and Adsorption Energy. The effect of surface termination for $Li_2Co_2O_4$ cubo-octahedrally shaped nanoparticles on the theoretical overpotential of the OER is illustrated in Table 2. Here, we only calculated the surface that has exposed cobalt ions. For the {110} facets, it was found that the overpotential of two terminations with different 4-fold coordinated configurations are 0.57 and 0.82 V, and the limited-rate steps are the oxidation of OH* and the formation of OH*, respectively. In contrast, the {100} facet with a 5-fold coordinated configuration has a lower overpotential of 0.38 V, and the formation of O_2 is thermodynamically limited by the oxidation of OH*, as shown in Figure 5. It is important at

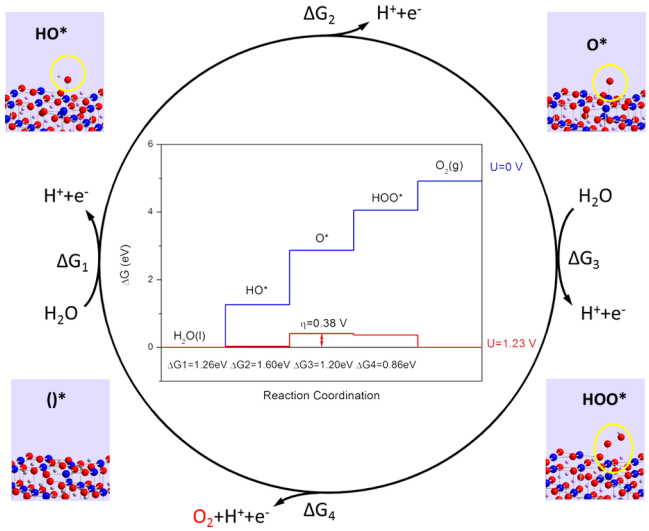

Figure 5. Schematic of the OER on the {100} surface. The inset plots the free-energy landscape. (Red spheres, oxygen; purple, lithium; blue, cobalt.)

this stage to compare our theoretical results to those of previous works on cobalt oxides due to the use of the same method and analogous calculated parameters. The overpotential of the {100} facet in $Li_2Co_2O_4$ is extensively superior to not only that of the {100} facet in a spinel Co_3O_4 system (0.48 V),[54] but also to that of the {104} facet in the layered β-CoOOH (0.48 V)[44] and γ-FeOOH (0.52 V).[55] In the reported studies, only the dual-metal systems β-$Ni_xCo_{1-x}OOH$ and FeW-doped CoOOH exhibit comparable performance, possessing overpotentials of 0.36 and 0.40 V, respectively.[44,56] These observations clearly demonstrate the pivotal role that the {100} facet plays in the OER activity for a nanosized $Li_2Co_2O_4$ system. Therefore, it is essential to determine the underlying cause.

It is well recognized that the activation energy for elementary surface reactions is strongly correlated with the affinity of a surface for a reagent.[57,58] Specific to OER, the activity can be plotted as a function of oxygen-binding energy.[59] For this reason, we calculated the adsorption energy between all the OER intermediates and the {100} facet, as well as two configurations of the {110} facet, as listed in Table 2. The binding abilities of the {100} facet and the {110} facet with a T2 configuration for O* species are very close, weaker than that of the {110} facet with T1 configurations, yielding to the substantial variance of the rate-limited step. This observation is consistent with the approved view that, when binding oxygen too strongly, the potential is imperfect by the formation of the HOO* species, whereas for surfaces that bind

DOI: 10.1021/acs.jpcc.8b00407
J. Phys. Chem. C 2018, 122, 14447−14458

oxygen too weakly, the potential is limited by the oxidation of OH*. Importantly, the free energy of forming OH* in the {100} facet is much closer to the optimal value of 1.23 eV, resulting in the best reactivity.

It is important to clarify the underlying mechanism for the outstanding OER performance, and especially that the 3d electron plays a crucial role in the OER process. To this end, we implemented an analysis based on the density of states (DOS) and Bader charge of the {100} facet at each step of the reaction. Figure 6 depicts the partial DOS of the Co 3d state.

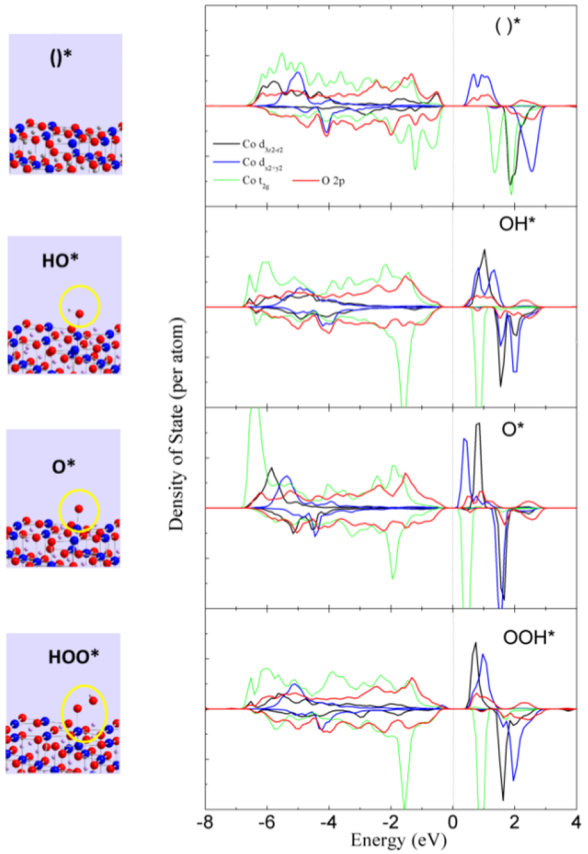

Figure 6. Density of states of the cobalt and oxygen participating in the OER at each step of the mechanism according to the scheme shown in Figure 5. (Red spheres, oxygen; purple, lithium; blue, cobalt.)

For a clean surface, the figure shows that the $3d_{z^2}$ orbit is a singlet occupied, whereas the $3d_{x^2-y^2}$ orbit is fully unoccupied, demonstrating an intermediate spin state of the Co^{3+} ions. Upon adsorption, the spin-up $3d_{z^2}$ state shifts up to above the Fermi level, whereas the other 3d states are nearly unchanged. This observation visibly indicates that the valence state of the surface cobalt ions transfers from a trivalent state to a tetravalent state once the binding of intermediates ensues, and, more importantly, only a singlet-occupied $3d_{z^2}$ orbit participates in the bonding process of all the reaction steps that donate the electron to the intermediates. The Bader charge analysis supports this conclusion by identifying a depletion of electronic charge upon adsorption, as listed in Table 3. Surprisingly, we found a reduction in the oxygen charge in the surface region, suggesting that lattice oxygens also contribute electrons in the reaction. This indicates there are both cathodic and anionic redox processes for the $Li_2Co_2O_4$ system, which is

Table 3. Calculated Bader Charge Analysis (in Units of Electrons) for the Co Empty Site as Well as for Co Sites Occupied by O, OH, and OOH on the {100} Surface of $Li_2Co_2O_4$

{100} surface	q(Co)	q($O_{surface}$)	q(adsorbate)
empty site (*)	1.48	−1.23	
O*	1.59	−1.17	−0.52
OH*	1.58	−1.17	−0.42
OOH*	1.57	−1.17	−0.21

consistent with the recent finding that shifting the oxygen p band closer to the Fermi level enhances the OER activity.[27,60]

3.5. Energy-Level Diagram of Spinel Trivalent Cobalt Oxides as a Function of Co−O Bond Length. We have discovered the IS-Co^{3+} ions in the {100} facet of $Li_2Co_2O_4$ and determined their dominant role in OER reactivity. However, the IS state of the trivalent cobalt ions is rare and its presence has been debated for a long time in the field of condensed-matter physics. Currently, a consensus has been reached that the ground state of Co^{3+} ions in an octahedron would never be an IS state. Few systems, such as $LaCoO_3$, possess a mixture of LS and HS states at room temperature, which was mistaken as the IS state. Recent works on OER catalysts proposed that the IS-Co^{3+} ions can be stabilized by the CoO_5 units that are induced by the oxygen vacancy at the surface. However, the available reports show that almost all of the trivalent cobalt oxides with bulk structure containing 5-fold coordination exhibit a HS state, such as the Sr_2CoO_3Cl system[36] and $BiCoO_3$, at ambient conditions.[37] These facts illustrate that the presence of IS-Co^{3+} requires a strictly coordinated symmetry and not just the CoO_5 units. Theoretically, the spin state of ions depends on the competition between the crystal field (10 Dq) and the intra-atomic exchange (J), as well as on the effect of the covalent bond related to the charge-transfer energy. For a Co^{3+} ion in an octahedron, it is well recognized that a transition from the LS to HS state occurs when 10 Dq < 2J.[61] When the apex atom is removed to form a CoO_5 unit, the 3d orbits split further, i.e., the energy of the d_{z^2} orbit would be pulled down and an expected IS state can appear when an electron transition from the d_{xy} orbit to the d_{z^2} orbit occurs in a suitable range of crystal field. Because the crystal-field strength is mainly determined by the bond length, identifying the characteristic structures, and especially the suitable Co−O distance range required to stabilize the IS-Co^{3+} ions, is mandatory.

To this end, the total energy-level diagram of the cobalt ions in the CoO_6 octahedra and the CoO_5 pyramids as a function of Co−O distance was determined by employing the configuration interaction cluster model method. Chen et al. used this method to successfully calculate an analogous diagram for the CoO_6 octahedron in a perovskite structure with the Co−O−Co bond angle of nearly 180°. Here, we used a charge-transfer energy Δ = 4.0 eV derived from the simulation of Co $L_{2,3}$-edge XAS. It is a typical value for the trivalent cobalt oxides with a bond angle of nearly 90°. First, we varied the Co−O_{api} distance but fixed the other Co−O distances to be 1.91 Å in the CoO_6 octahedral cluster, as shown in Figure 7a. It was found that the energy of the LS configuration sharply increases with increasing Co−O_{api} distance. When the Co−O_{api} distance is increased to 2.4 Å, there is a crossover between the LS and HS state. Further increasing the Co−O_{api} distance to 3.5 Å, the IS configuration can become the ground state. Clearly, this

DOI: 10.1021/acs.jpcc.8b00407
J. Phys. Chem. C 2018, 122, 14447−14458

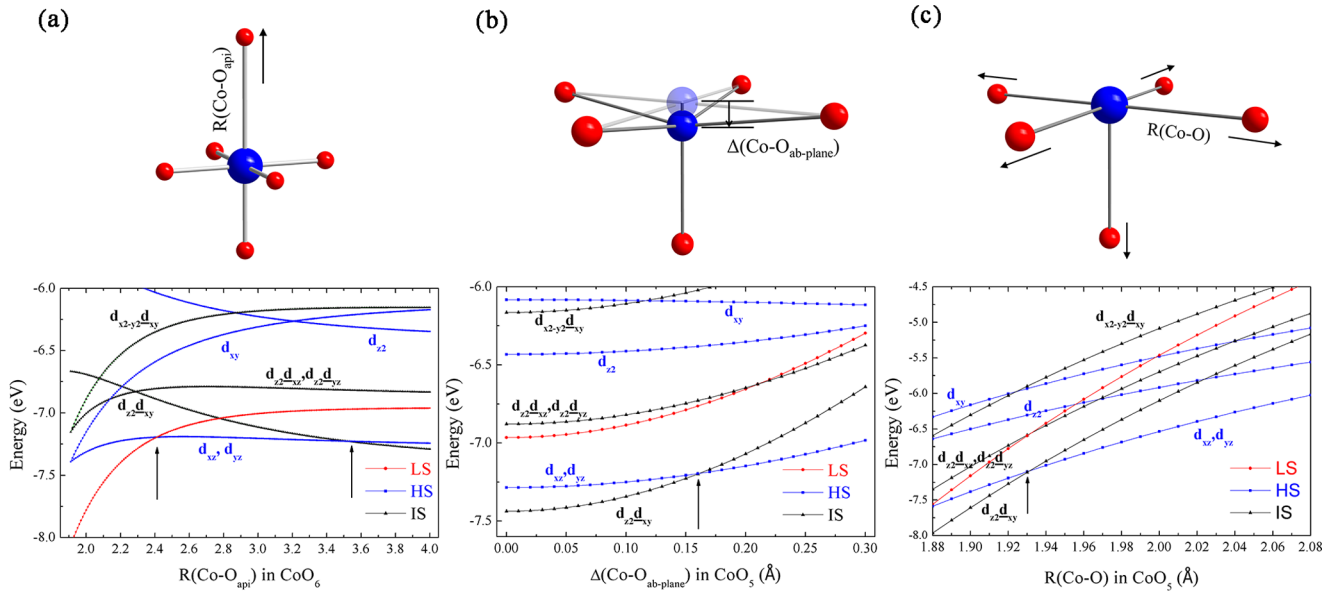

Figure 7. Spin-correlated energy-level diagram as a function of (a) the Co−O_{api} distance in the CoO_6 octahedral cluster, (b) the displacement of Co from the O_{ab}-plane, and (c) the Co−O distance in the CoO_5 square-pyramidal cluster. The corresponding schematics of the cluster−structure changes are shown on top. (Red spheres, oxygen; blue, cobalt.)

demonstrates that the IS ground state can be stabilized by a CoO_5 square-pyramidal structure, agreeing well with the result of our DFT calculation. Unfortunately, the most of the 5-fold-coordinated cobalt oxides possess the distorted CoO_5 structure in which a Co ion deviates from the basal CoO_4 plane, resulting in the energy lowering of the $3d_{x^2-y^2}$ orbit and, in turn, a HS ground state. Our calculation identified this transition point to be at 0.15 Å for the out-of-basal-plane Co displacements, as shown in Figure 7b. Finally, Figure 7c describes the evolution of a spin state as a function of the Co−O distance for the CoO_5 square-pyramidal structure. It is important to find that a crossover between the IS and the HS states occurs at 1.93 Å and that the IS state can become a ground state in the short Co−O bond length region. According to the above calculations, we point out that both CoO_5 square-pyramidal symmetry and short Co−O bond length are essential for the presence of IS-Co^{3+} ions. This rigorous requirement implies that it is difficult for most of the nanoparticles on the surface to stabilize the Co^{3+}-IS state due to the large structural reconstruction. In terms of our finding on the {100} facet of $Li_2Co_2O_4$, we found that its nonpolar character yields a small surface distortion, thus playing a significant role in the presence of IS-Co^{3+} ions. More importantly, bearing in mind the universality of our calculational result, this diagram is appropriate for all of the edge-sharing cobalt-based oxides possessing a Co−O−Co bond angle of 90°, such as layered oxides and oxyhydroxides. This can be seen in the finding for layered $LiCoO_2$, in which the IS-Co^{3+} ions were found in the {104} facet, which is a nonpolar surface that also contains a CoO_5 square-pyramidal motif.[39]

3.6. Correlation between OER Performance and Co 3d−O 2p Hybridization. Although surface IS-Co^{3+} ions play a significant role in OER performance, the DFT calculation also revealed the charge depletion of oxygen ions upon reactant adsorption, illustrating that they participate in the OER process together with cobalt ions. This finding can be well understood by molecular orbital theory. In fact, the electronic states near the Fermi level play an integral role in catalyzing oxygen, especially for the OER.[62] Specific to the {100} facet in a $Li_2Co_2O_4$ catalyst, it is the e_g* antibonding orbit that is a major contributor from the Co $3d_{z^2}$ state and a minor one from the O 2p state, as shown in Figure 8. The

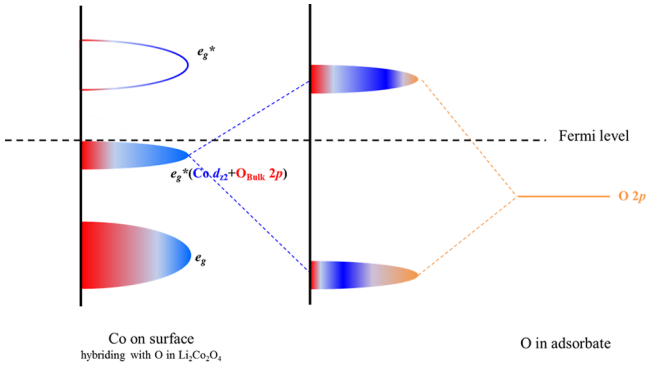

Figure 8. Schematic of the formation of a bond between an oxygen adsorbate level and the molecular orbits of the oxide.

interaction between surface and reactants strongly depends on this molecular orbit. For this reason, cobalt and oxygen together afford a charge variation during OER cycling. In addition, an antibonding orbit possesses a more extended spatial distribution than a bonding state, and it would be further enhanced when mixing with an O 2p state. Such an extended wave function facilitates the binding ability for reactants.

We have noted that correlated oxygen is involved in the OER process with a strong Co 3d−O 2p hybridization. On the other hand, this issue can be reflected by the electronic ground state of cobalt ions, φ = 54.6%|$3d^6$ > +40.5%|$3d^7\underline{L}$ > +4.9%|$3d^8\underline{L}^2$> ($\underline{L}$ represents ligand hole), obtained by the simulation performed for Co $L_{2,3}$ edge XAS data as shown in Figure S8. It is notable that the ground state has a significant weight of $3d^7\underline{L}$ and $3d^8\underline{L}^2$ components. This highly Co 3d−O 2p hybridization effect can be quantified by $3d_{z^2}$ electron occupancy. On the

DOI: 10.1021/acs.jpcc.8b00407
J. Phys. Chem. C 2018, 122, 14447−14458

basis of this ground state, we accurately determined it to be $t_{2g}^{5}d_{z^2}^{1.1}$ $d_{x^2-y^2}^{0.4}$ of cobalt ions in the {100} facet of $Li_2Co_2O_4$. In 2011, Shao-Horn and co-workers proposed that the e_g filling number plays an integral role in OER reactivity, and further pointed out that the optimal value is $e_g^{1.2}$. Later, this proposal became a widely accepted design principle for OER catalysts. However, several works provide a distinct understanding regarding this fractional occupancy of the e_g orbit. Some investigations realized that it is ascribed to the mixing of Co^{2+} and Co^{3+} ions,[28,29] whereas other studies regarded it as the mixing of HS and LS states of the Co^{3+} ion.[63] Herein, we clarify that this fractional e_g filling fundamentally arises from the highly covalent nature of the Co^{3+}−O bond, involving the significantly O 2p component. Our understanding is well supported by the recent observations that the OER performance can be controlled by the Co−O bond length[27] and the anionic process in this cycling process.[60] In brief, we illustrate that, for trivalent cobalt oxides, the IS state and suitable d−p hybridization strength are the ingredients for producing a desirable $3d_{z^2}$ occupancy, and, in turn, excellent OER activity.

4. CONCLUSIONS

In this work, we unraveled that the OER activity of Co^{3+} ions in a cubo-octahedral shape nanosized spinel $Li_2Co_2O_4$ exhibits surface dependence owing to the variability of its electronic configurations. The DFT calculation shows that the {100} surface containing the unusual Co^{3+}-IS state presents an impressive intrinsic activity, which is superior to that of the other two surfaces. Using high-resolution advanced X-ray techniques combined with ab initio modeling, we obtained the spin-correlated energy-level diagram as a function of the Co−O bond length, determining the precondition of the occurrence of the Co^{3+}-IS state in edge-sharing systems, i.e., the square-pyramidal CoO_5 structure and the short Co−O bond length (<1.93 Å) are essential. Our study highlights the importance of the nonpolar-character facet for the existence of CoO_5 square-pyramidal units. In view of the documented data of the Co−O bond length, we certainly deduced that the {100} crystal plane in spinel oxides and the {104} crystal plane in layered oxides and oxyhydroxides would contain IS-Co^{3+} ions. Especially, we found that the lattice oxygen behaves as a partner in cationic redox couples. This effect could be understood by the strong Co 3d−O 2p hybridization, which produces the $3d_{z^2}^{1.1}$ occupancy of cobalt ions. This covalent model provides a better insight into the origin of fractional occupancy of the Co 3d state, whereas conventional ionic picture shows that it arises from the mixed Co^{2+}/Co^{3+} ions. Our study proposes a direct guideline for designing an efficient cobalt-based OER catalysts, i.e., by synthesizing the nanosized system with a high-percentage facet that contains CoO_5 square-pyramidal units of short bond length and tuning the covalency of the Co−O bond to obtain the desirable $3d_{z^2}$ filling.

■ ASSOCIATED CONTENT

Supporting Information

The Supporting Information is available free of charge on the ACS Publications website at DOI: 10.1021/acs.jpcc.8b00407.

X-ray diffraction refinement, fitting for EXAFS, XPS, XAS simulation, and SQUID data (PDF)

■ AUTHOR INFORMATION

Corresponding Authors

*E-mail: wangjianqiang@sinap.ac.cn (J.W.).
*E-mail: zhangshuo@sinap.ac.cn (S.Z.).

ORCID

Jianqiang Wang: 0000-0003-4123-7592
Shuo Zhang: 0000-0002-3715-8632

Author Contributions

⊥J.L. and J.Z. contributed equally.

Notes

The authors declare no competing financial interest.

■ ACKNOWLEDGMENTS

This work was partly supported by the National Natural Science Foundation of China (Grant Nos. 11305250 and 11575280), the Joint Funds of the National Natural Science Foundation of China (Grant Nos. U1232117 and U1232204), and the Key Project of Science and Technology of Shanghai (Grant No. 15DZ1200100).

■ REFERENCES

(1) Gasteiger, H. A.; Marković, N. M. Just a Dream—or Future Reality? *Science* **2009**, *324*, 48−49.
(2) Ormerod, R. M. Solid Oxide Fuel Cells. *Chem. Soc. Rev.* **2003**, *32*, 17−28.
(3) Armand, M.; Tarascon, J. M. Building Better Batteries. *Nature* **2008**, *451*, 652−657.
(4) Katsounaros, I.; Cherevko, S.; Zeradjanin, A. R.; Mayrhofer, K. J. J. Oxygen Electrochemistry as a Cornerstone for Sustainable Energy Conversion. *Angew. Chem., Int. Ed.* **2014**, *53*, 102−121.
(5) Seh, Z. W.; Kibsgaard, J.; Dickens, C. F.; Chorkendorff, I.; Nørskov, J. K.; Jaramillo, T. F. Combining Theory and Experiment in Electrocatalysis: Insights into Materials Design. *Science* **2017**, *355*, No. eaad4998.
(6) Kärkäs, M. D.; Verho, O.; Johnston, E. V.; Åkermark, B. Artificial Photosynthesis: Molecular Systems for Catalytic Water Oxidation. *Chem. Rev.* **2014**, *114*, 11863−12001.
(7) Chen, S.; Qiao, S.-Z. Hierarchically Porous Nitrogen-Doped Graphene−$NiCo_2O_4$ Hybrid Paper as an Advanced Electrocatalytic Water-Splitting Material. *ACS Nano* **2013**, *7*, 10190−10196.
(8) Cui, B.; Lin, H.; Li, J.-B.; Li, X.; Yang, J.; Tao, J. Core−Ring Structured $NiCo_2O_4$ Nanoplatelets: Synthesis, Characterization, and Electrocatalytic Applications. *Adv. Funct. Mater.* **2008**, *18*, 1440−1447.
(9) Li, Y.; Hasin, P.; Wu, Y. $Ni_xCo_{3-x}O_4$ Nanowire Arrays for Electrocatalytic Oxygen Evolution. *Adv. Mater.* **2010**, *22*, 1926−1929.
(10) Liang, Y.; Wang, H.; Zhou, J.; Li, Y.; Wang, J.; Regier, T.; Dai, H. Covalent Hybrid of Spinel Manganese−Cobalt Oxide and Graphene as Advanced Oxygen Reduction Electrocatalysts. *J. Am. Chem. Soc.* **2012**, *134*, 3517−3523.
(11) Li, C.; Han, X.; Cheng, F.; Hu, Y.; Chen, C.; Chen, J. Phase and Composition Controllable Synthesis of Cobalt Manganese Spinel Nanoparticles towards Efficient Oxygen Electrocatalysis. *Nat. Commun.* **2015**, *6*, No. 7345.
(12) Jiao, F.; Frei, H. Nanostructured Cobalt Oxide Clusters in Mesoporous Silica as Efficient Oxygen-Evolving Catalysts. *Angew. Chem., Int. Ed.* **2009**, *48*, 1841−1844.
(13) Rosen, J.; Hutchings, G. S.; Jiao, F. Ordered Mesoporous Cobalt Oxide as Highly Efficient Oxygen Evolution Catalyst. *J. Am. Chem. Soc.* **2013**, *135*, 4516−4521.
(14) Tung, C.-W.; Hsu, Y.-Y.; Shen, Y.-P.; Zheng, Y.; Chan, T.-S.; Sheu, H.-S.; Cheng, Y.-C.; Chen, H. M. Reversible Adapting Layer Produces Robust Single-crystal Electrocatalyst for Oxygen Evolution. *Nat. Commun.* **2015**, *6*, No. 8106.
(15) Gardner, G. P.; Go, Y. B.; Robinson, D. M.; Smith, P. F.; Hadermann, J.; Abakumov, A.; Greenblatt, M.; Dismukes, G. C.

DOI: 10.1021/acs.jpcc.8b00407
J. Phys. Chem. C 2018, 122, 14447−14458

Structural Requirements in Lithium Cobalt Oxides for the Catalytic Oxidation of Water. *Angew. Chem., Int. Ed.* **2012**, *51*, 1616−1619.
(16) Maiyalagan, T.; Jarvis, K. A.; Therese, S.; Ferreira, P. J.; Manthiram, A. Spinel-type Lithium Cobalt Oxide as a Bifunctional Electrocatalyst for the Oxygen Evolution and Oxygen Reduction Reactions. *Nat. Commun.* **2014**, *5*, No. 3949.
(17) Maitra, U.; Naidu, B. S.; Govindaraj, A.; Rao, C. N. Importance of Trivalency and the e_g^1 Configuration in the Photocatalytic Oxidation of Water by Mn and Co Oxides. *Proc. Natl. Acad. Sci. U.S.A.* **2013**, *110*, 11704−11707.
(18) Bao, J.; Zhang, X.; Fan, B.; Zhang, J.; Zhou, M.; Yang, W.; Hu, X.; Wang, H.; Pan, B.; Xie, Y. Ultrathin Spinel-Structured Nanosheets Rich in Oxygen Deficiencies for Enhanced Electrocatalytic Water Oxidation. *Angew. Chem.* **2015**, *127*, 7507−7512.
(19) Hutchings, G. S.; Zhang, Y.; Li, J.; Yonemoto, B. T.; Zhou, X.; Zhu, K.; Jiao, F. In Situ Formation of Cobalt Oxide Nanocubanes as Efficient Oxygen Evolution Catalysts. *J. Am. Chem. Soc.* **2015**, *137*, 4223−4229.
(20) Ma, T. Y.; Dai, S.; Jaroniec, M.; Qiao, S. Z. Metal−Organic Framework Derived Hybrid Co_3O_4-Carbon Porous Nanowire Arrays as Reversible Oxygen Evolution Electrodes. *J. Am. Chem. Soc.* **2014**, *136*, 13925−13931.
(21) Tian, N.; Zhou, Z.-Y.; Sun, S.-G.; Ding, Y.; Wang, Z. L. Synthesis of Tetrahexahedral Platinum Nanocrystals with High-Index Facets and High Electro-Oxidation Activity. *Science* **2007**, *316*, 732−735.
(22) Hu, L.; Peng, Q.; Li, Y. Selective Synthesis of Co_3O_4 Nanocrystal with Different Shape and Crystal Plane Effect on Catalytic Property for Methane Combustion. *J. Am. Chem. Soc.* **2008**, *130*, 16136−16137.
(23) Zhou, K.; Li, Y. Catalysis Based on Nanocrystals with Well-Defined Facets. *Angew. Chem., Int. Ed.* **2012**, *51*, 602−613.
(24) Hammer, B.; Nørskov, J. K. Theoretical Surface Science and Catalysis—Calculations and Concepts. In *Advances in Catalysis*; Academic Press: 2000; Vol. *45*, pp 71−129.
(25) Suntivich, J.; May, K. J.; Gasteiger, H. A.; Goodenough, J. B.; Shao-Horn, Y. A Perovskite Oxide Optimized for Oxygen Evolution Catalysis from Molecular Orbital Principles. *Science* **2011**, *334*, 1383−1385.
(26) Suntivich, J.; Gasteiger, H. A.; Yabuuchi, N.; Nakanishi, H.; Goodenough, J. B.; Shao-Horn, Y. Design Principles for Oxygen-Reduction Activity on Perovskite Oxide Catalysts for Fuel Cells and Metal−Air Batteries. *Nat. Chem.* **2011**, *3*, 546−550.
(27) Grimaud, A.; May, K. J.; Carlton, C. E.; Lee, Y.-L.; Risch, M.; Hong, W. T.; Zhou, J.; Shao-Horn, Y. Double Perovskites as a Family of Highly Active Catalysts for Oxygen Evolution in Alkaline Solution. *Nat. Commun.* **2013**, *4*, No. 2439.
(28) Huang, J.; Chen, J.; Yao, T.; He, J.; Jiang, S.; Sun, Z.; Liu, Q.; Cheng, W.; Hu, F.; Jiang, Y.; et al. CoOOH Nanosheets with High Mass Activity for Water Oxidation. *Angew. Chem.* **2015**, *127*, 8846−8851.
(29) Zhu, Y.; Zhou, W.; Chen, Z.-G.; Chen, Y.; Su, C.; Tadé, M. O.; Shao, Z. $SrNb_{0.1}Co_{0.7}Fe_{0.2}O_{3-\delta}$ Perovskite as a Next-Generation Electrocatalyst for Oxygen Evolution in Alkaline Solution. *Angew. Chem., Int. Ed.* **2015**, *54*, 3897−3901.
(30) Imada, M.; Fujimori, A.; Tokura, Y. Metal-Insulator Transitions. *Rev. Mod. Phys.* **1998**, *70*, 1039−1263.
(31) Wu, W. B.; Huang, D. J.; Okamoto, J.; Tanaka, A.; Lin, H. J.; Chou, F. C.; Fujimori, A.; Chen, C. T. Orbital Symmetry and Electron Correlation in Na_xCoO_2. *Phys. Rev. Lett.* **2005**, *94*, No. 146402.
(32) Mizokawa, T.; Wakisaka, Y.; Sudayama, T.; Iwai, C.; Miyoshi, K.; Takeuchi, J.; Wadati, H.; Hawthorn, D. G.; Regier, T. Z.; Sawatzky, G. A. Role of Oxygen Holes in Li_xCoO_2 Revealed by Soft X-Ray Spectroscopy. *Phys. Rev. Lett.* **2013**, *111*, No. 056404.
(33) Chang, C. F.; Hu, Z.; Wu, H.; Burnus, T.; Hollmann, N.; Benomar, M.; Lorenz, T.; Tanaka, A.; Lin, H. J.; Hsieh, H. H.; et al. Spin Blockade, Orbital Occupation, and Charge Ordering in $La_{1.5}Sr_{0.5}CoO_4$. *Phys. Rev. Lett.* **2009**, *102*, No. 116401.
(34) Chen, J. M.; Chin, Y. Y.; Valldor, M.; Hu, Z.; Lee, J. M.; Haw, S. C.; Hiraoka, N.; Ishii, H.; Pao, C. W.; Tsuei, K. D.; et al. A Complete High-to-Low Spin State Transition of Trivalent Cobalt Ion in Octahedral Symmetry in $SrCo_{0.5}Ru_{0.5}O_{3-\delta}$. *J. Am. Chem. Soc.* **2014**, *136*, 1514−1519.
(35) Hollmann, N.; Hu, Z.; Valldor, M.; Maignan, A.; Tanaka, A.; Hsieh, H. H.; Lin, H. J.; Chen, C. T.; Tjeng, L. H. Electronic and Magnetic Properties of the Kagome Systems $YBaCo_4O_7$ and $YBaCo_3MO_7$ (M = Al, Fe). *Phys. Rev. B* **2009**, *80*, No. 085111.
(36) Hu, Z.; Wu, H.; Haverkort, M.; Hsieh, H.; Lin, H.; Lorenz, T.; Baier, J.; Reichl, A.; Bonn, I.; Felser, C.; et al. Different Look at the Spin State of Co^{3+} Ions in a CoO_5 Pyramidal Coordination. *Phys. Rev. Lett.* **2004**, *92*, No. 207402.
(37) Oka, K.; Azuma, M.; Chen, W.-t.; Yusa, H.; Belik, A. A.; Takayama-Muromachi, E.; Mizumaki, M.; Ishimatsu, N.; Hiraoka, N.; Tsujimoto, M.; et al. Pressure-Induced Spin-State Transition in $BiCoO_3$. *J. Am. Chem. Soc.* **2010**, *132*, 9438−9443.
(38) Maram, P. S.; Costa, G. C.; Navrotsky, A. Experimental Confirmation of Low Surface Energy in $LiCoO_2$ and Implications for Lithium Battery Electrodes. *Angew. Chem., Int. Ed.* **2013**, *52*, 12139−12142.
(39) Qian, D.; Hinuma, Y.; Chen, H.; Du, L. S.; Carroll, K. J.; Ceder, G.; Grey, C. P.; Meng, Y. S. Electronic Spin Transition in Nanosize Stoichiometric Lithium Cobalt Oxide. *J. Am. Chem. Soc.* **2012**, *134*, 6096−6099.
(40) Chen, J.; Selloni, A. Electronic States and Magnetic Structure at the Co_3O_4 (110) Surface: A First-Principles Study. *Phys. Rev. B* **2012**, *85*, No. 085306.
(41) Xiao, X.; Liu, X.; Zhao, H.; Chen, D.; Liu, F.; Xiang, J.; Hu, Z.; Li, Y. Facile Shape Control of Co_3O_4 and the Effect of the Crystal Plane on Electrochemical Performance. *Adv. Mater.* **2012**, *24*, 5762−5766.
(42) Kresse, G.; Furthmüller, J. Efficient Iterative Schemes for *Ab Initio* Total-Energy Calculations using a Plane-Wave Basis Set. *Phys. Rev. B* **1996**, *54*, 11169−11186.
(43) Kresse, G.; Joubert, D. From Ultrasoft Pseudopotentials to the Projector Augmented-Wave Method. *Phys. Rev. B* **1999**, *59*, 1758−1775.
(44) Bajdich, M.; Garcia-Mota, M.; Vojvodic, A.; Norskov, J. K.; Bell, A. T. Theoretical Investigation of the Activity of Cobalt Oxides for the Electrochemical Oxidation of Water. *J. Am. Chem. Soc.* **2013**, *135*, 13521−13530.
(45) de Groot, F. M. F. X-ray Absorption and Dichroism of Transition Metals and Their Compounds. *J. Electron Spectrosc. Relat. Phenom.* **1994**, *67*, 529−622.
(46) Porthault, H.; Baddour-Hadjean, R.; Le Cras, F.; Bourbon, C.; Franger, S. Raman Study of the Spinel-to-Layered Phase Transformation in Sol−Gel $LiCoO_2$ Cathode Powders as a Function of the Post-Annealing Temperature. *Vib. Spectrosc.* **2012**, *62*, 152−158.
(47) Radaelli, P. G.; Cheong, S. W. Structural phenomena associated with the spin-state transition in $LaCoO_3$. *Phys. Rev. B* **2002**, *66*, No. 094408.
(48) Marianetti, C. A.; Kotliar, G.; Ceder, G. A first-Order Mott Transition in Li_xCoO_2. *Nat. Mater.* **2004**, *3*, 627−631.
(49) Wu, H.; Haverkort, M. W.; Hu, Z.; Khomskii, D. I.; Tjeng, L. H. Nature of Magnetism in $Ca_3Co_2O_6$. *Phys. Rev. Lett.* **2005**, *95*, No. 186401.
(50) de Groot, F.; Vanko, G.; Glatzel, P. The 1s X-ray Absorption Pre-Edge Structures in Transition Metal Oxides. *J. Phys.: Condens. Matter* **2009**, *21*, No. 104207.
(51) de Groot, F. M. F.; Fuggle, J. C.; Thole, B. T.; Sawatzky, G. A. $L_{2,3}$ X-Ray-Absorption Edges of d^0 Compounds: K^+, Ca^{2+}, Sc^{3+}, and Ti^{4+} in Oh (Octahedral) Symmetry. *Phys. Rev. B* **1990**, *41*, 928−937.
(52) Lin, H. J.; Chin, Y. Y.; Hu, Z.; Shu, G. J.; Chou, F. C.; Ohta, H.; Yoshimura, K.; Hébert, S.; Maignan, A.; Tanaka, A.; et al. Local Orbital Occupation and Energy Levels of Co in Na_xCoO_2: A Soft X-Ray Absorption Study. *Phys. Rev. B* **2010**, *81*, No. 115138.
(53) Wu, H.; Hu, Z.; Burnus, T.; Denlinger, J. D.; Khalifah, P. G.; Mandrus, D. G.; Jang, L. Y.; Hsieh, H. H.; Tanaka, A.; Liang, K. S.;

DOI: 10.1021/acs.jpcc.8b00407
J. Phys. Chem. C 2018, 122, 14447−14458

et al. Orbitally Driven Spin-Singlet Dimerization in S = 1 $La_4Ru_2O_{10}$. *Phys. Rev. Lett.* **2006**, *96*, No. 256402.
(54) Plaisance, C. P.; van Santen, R. A. Structure Sensitivity of the Oxygen Evolution Reaction Catalyzed by Cobalt(II,III) Oxide. *J. Am. Chem. Soc.* **2015**, *137*, 14660−14672.
(55) Friebel, D.; Louie, M. W.; Bajdich, M.; Sanwald, K. E.; Cai, Y.; Wise, A. M.; Cheng, M.-J.; Sokaras, D.; Weng, T.-C.; Alonso-Mori, R.; et al. Identification of Highly Active Fe Sites in (Ni,Fe)OOH for Electrocatalytic Water Splitting. *J. Am. Chem. Soc.* **2015**, *137*, 1305−1313.
(56) Zhang, B.; Zheng, X.; Voznyy, O.; Comin, R.; Bajdich, M.; Garcia-Melchor, M.; Han, L.; Xu, J.; Liu, M.; Zheng, L.; et al. Homogeneously Dispersed Multimetal Oxygen-Evolving Catalysts. *Science* **2016**, *352*, 333−337.
(57) Nørskov, J. K.; Bligaard, T.; Rossmeisl, J.; Christensen, C. H. Towards the Computational Design of Solid Catalysts. *Nat. Chem.* **2009**, *1*, 37−46.
(58) Stamenkovic, V.; Mun, B. S.; Mayrhofer, K. J. J.; Ross, P. N.; Markovic, N. M.; Rossmeisl, J.; Greeley, J.; Nørskov, J. K. Changing the Activity of Electrocatalysts for Oxygen Reduction by Tuning the Surface Electronic Structure. *Angew. Chem.* **2006**, *118*, 2963−2967.
(59) Man, I. C.; Su, H.-Y.; Calle-Vallejo, F.; Hansen, H. A.; Martínez, J. I.; Inoglu, N. G.; Kitchin, J.; Jaramillo, T. F.; Nørskov, J. K.; Rossmeisl, J. Universality in Oxygen Evolution Electrocatalysis on Oxide Surfaces. *ChemCatChem* **2011**, *3*, 1159−1165.
(60) Grimaud, A.; Hong, W. T.; Shao-Horn, Y.; Tarascon, J. M. Anionic Redox Processes for Electrochemical Devices. *Nat. Mater.* **2016**, *15*, 121−126.
(61) Potze, R. H.; Sawatzky, G. A.; Abbate, M. Possibility for an Intermediate-Spin Ground State in the Charge-Transfer Material $SrCoO_3$. *Phys. Rev. B* **1995**, *51*, 11501−11506.
(62) Vojvodic, A.; Norskov, J. K. Optimizing Perovskites for the Water-Splitting Reaction. *Science* **2011**, *334*, 1355−1356.
(63) Zhou, S.; Miao, X.; Zhao, X.; Ma, C.; Qiu, Y.; Hu, Z.; Zhao, J.; Shi, L.; Zeng, J. Engineering Electrocatalytic Activity in Nanosized Perovskite Cobaltite through Surface Spin-State Transition. *Nat. Commun.* **2016**, *7*, No. 11510.

DOI: 10.1021/acs.jpcc.8b00407
J. Phys. Chem. C 2018, 122, 14447−14458